CHEMISTRY OF MATERIALS

pubs.acs.org/cm Article

# Growth of Multilayer Graphene with a Built-in Vertical Electric Field

Min Seok Yoo,‡ Hyo Chan Lee,‡ Christoph Wolf, Nguyen Ngan Nguyen, Do-Hyun Park, Jinsung Kim, Eunho Lee, Hyun-Jong Chung, and Kilwon Cho*

Cite This: https://dx.doi.org/10.1021/acs.chemmater.0c01145 Read Online

ACCESS | Metrics & More | Article Recommendations | Supporting Information

**ABSTRACT:** Multilayer graphene is considered a promising material for various optoelectronic devices. To exploit its intriguing electronic properties, an electric field must be achieved inside this material. However, creation of a desired electric field in multilayer graphene is difficult because any external electric field is mostly screened by its outermost surface. Here, we report a one-step chemical vapor deposition method for the synthesis of Bernal-like stacked graphene with a built-in vertical electric field that can be tuned over a wide range. This method can be used to control the optoelectronic properties of graphene in the synthesis stage. Owing to this built-in vertical electric field and Bernal-like stacking, the synthesized graphene exhibits vertical photovoltaic effects, which is very promising for various optoelectronic applications.

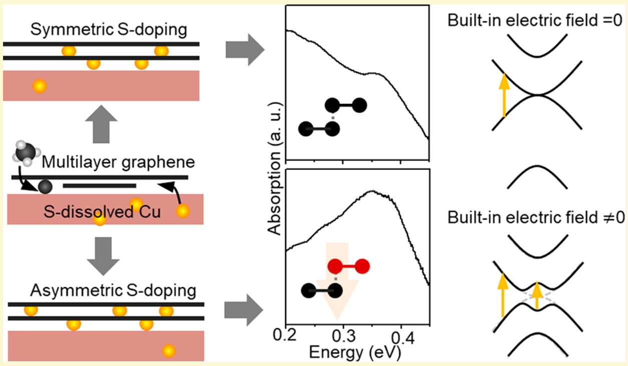

## INTRODUCTION

Graphene is a two-dimensional carbon material with a high charge-carrier mobility, a high thermal conductivity, and a high Young's modulus.[1−3] When graphene layers are stacked, a distinctive electronic structure develops that depends on the number of graphene layers and the stacking order and that preserves the superior properties of single-layer graphene.[4−9] The most intriguing property of MLG is that its electronic structure can be further tuned by generating differences between the electrostatic energies of the graphene layers; whereas single-layer graphene is a gapless semimetal, MLG has a band gap under a vertical electric-field (E-field).[10−13] For these reasons, MLG is a promising material for a wide range of optoelectronic applications.[14−17]

Despite this potential of MLG, its use in optoelectronic applications has been limited by the difficulty of synthesizing large-area MLG with a uniform stacking order.[18−22] Moreover, the challenge of introducing a high E-field inside MLG to tune the electronic structure remains unsolved. The control of the electronic structure of MLG has been achieved mainly by fabricating dual-gate field-effect transistors (FETs),[11] but this approach is not readily applicable to the fabrication of complex MLG-based integrated circuits. Postgrowth chemical doping of MLG surfaces has also been performed in attempts to control the MLG electronic structure,[23−25] but such doping is limited to the graphene layers nearest and next-nearest to the dopant materials due to the interlayer screening effect.[26] In addition, the MLG prepared through postgrowth chemical doping is unstable to air exposure, humidity, and thermal annealing. Here, we report a chemical vapor deposition (CVD) method for the synthesis of Bernal-like stacked MLG with a built-in vertical E-field. Using sulfurized Cu (S−Cu) as the catalyst, our method enables the synthesis of MLG with an S-doping gradient that provides a built-in E-field and thus modifies the electronic structure of graphene. Owing to the high built-in E-field and Bernal-like stacking, a photovoltaic current arises in the bulk region of S-graphene under continuous-wave illumination.

## RESULTS AND DISCUSSION

**Strategy for the Synthesis of Bernal-Like Stacked MLG with a Built-in E-Field.** We synthesized S-doped multilayer graphene (S-graphene) on a sulfur-dissolved Cu foil (S−Cu) (Figure 1a and Figure S1). The cross-sectional transmission electron microscopy (TEM) image in Figure 1b shows that the S-graphene is multilayer, in contrast to the monolayer graphene grown on untreated Cu foil (Figure S2). The sulfur electron energy loss spectroscopy (EELS) map of the S-graphene for the same region (Figure 1b) shows that the S atoms are dispersed through all layers of the S-graphene sample. In particular, more S atoms are present in the upper layer than in the lower layer. The top-view S-EELS map in Figure S3 shows that the S atoms are uniformly distributed in the in-plane direction. The selective area electron diffraction

Received: March 16, 2020
Revised: May 25, 2020
Published: May 26, 2020

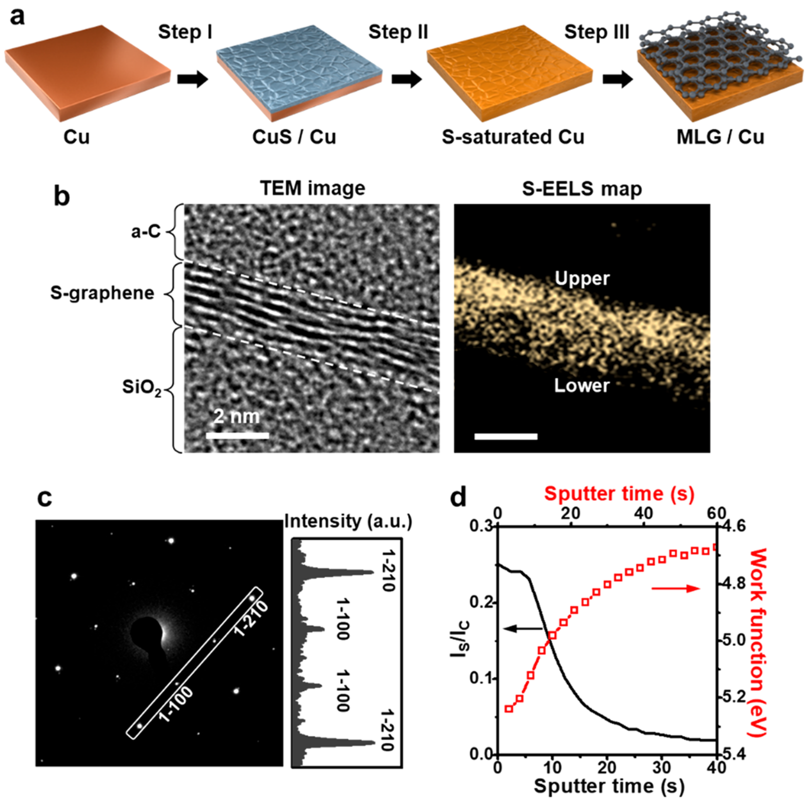

**Figure 1.** Synthesis of MLG on S-Cu foil. (a) Schematic diagram of graphene growth. Step I: sulfurization of Cu. Step II: $H_2$ annealing of S-Cu. Step III: graphene growth. (b) Cross-sectional TEM image (left) and S-EELS map (right) of S-graphene transferred onto a $SiO_2$ substrate. (c) SAED pattern of graphene. (d) SIMS depth profile of the S atoms in S-graphene, and work function depth profile estimated with UPS.

(SAED) pattern of S-graphene (Figure 1c and Figure S4) is hexagonal with a low misorientation angle of <3°. The (1−210) spot is more intense than the (1−100) spot; this difference demonstrates that the stacking order of the synthesized S-graphene is close to that of Bernal stacking.[27] We conducted a Raman spectroscopic analysis of S-graphene by obtaining a large-area Raman map (200 $\mu$m × 200 $\mu$m) with a 532 nm laser (Supplementary Figure 5a and 5b). The average Raman spectrum shows signature peaks of graphene (the D, G, and 2D peaks). The $I_D/I_G$ ratio is 0.1, which corresponds to a defect density of $5.0 \times 10^{-4}$ atom %.[28] The $I_D/I_{D'}$ ratio of less than 7 indicates that the D peak is mainly due to vacancies rather than sp3-type defect.[29] At room temperature, S-graphene transferred onto hexagonal boron nitride (hBN) exhibits a charge carrier mobility of ~10 000 $cm^2\ V^{-1}\ s^{-1}$ (Figure S5c and S5d).

The time-of-flight secondary ion mass spectrometry (TOF-SIMS) depth profile and the ultraviolet photoelectron spectroscopy (UPS) depth profile in Figure 1d suggest the presence of a vertical gradient in the doping of the S atoms in S-graphene. The $I_S/I_C$ ratio decreases as the $Cs^+$ ion sputtering time increases (Figure S6); this result is consistent with the S-EELS map. In addition to the gradient in the S content of S-graphene, there is a gradient in the work function along the *c* axis, which generates a built-in vertical E-field in S-graphene (Figure S7). The relationship between the S content and the work function indicates that the intercalated S atoms induce the hole doping of graphene.

To investigate the mechanism of S-graphene growth, we used isotopic labeling of the $CH_4$ precursor. Graphene was synthesized by the sequential introduction of 50 sccm $^{12}CH_4$ for 15 min and $^{13}CH_4$ for 5 min. The injection of 50 sccm $CH_4$ for 15 min was found to be sufficient for fully covering the Cu surface with one layer of graphene. The TOF-SIMS spectrum and depth profile of the resulting S-graphene shown in Figure 2a indicate that the introduced $^{12}CH_4$ was initially consumed to form the uppermost full-coverage graphene layer and that the $^{13}CH_4$ introduced later formed the lower graphene layer.

In the Raman maps (Figure 2b) of the $^{12}$G peak (~1600 $cm^{-1}$) and the $^{13}$G peak (~1540 $cm^{-1}$), the $^{12}$G peak was observed across the whole scanned region whereas the $^{13}$G peak was observed in only specific regions. Alternative patterns of the $^{12}$G and $^{13}$G peaks signify that the adlayer S-graphene was grown by surface-mediated reaction on S−Cu and not by the precipitation of C atoms during the cooling stage. These results suggest that the upper layer of graphene did not inhibit the penetration of $CH_4$ molecules, so MLG formed below the upper layer of graphene.

To determine how Cu sulfurization affects graphene growth, we used TOF-SIMS, high-resolution TEM (HR-TEM), and energy-dispersive X-ray spectroscopy to identify the chemical state of the Cu catalyst during CVD (Figures S8 and S9). During $H_2$ annealing prior to graphene growth, the initial CuS layer on Cu foil would turn to a $Cu_2S$ layer, gradually thinned, and eventually disappeared completely after $H_2$ annealing for 15 min (Figure S8). During the initial stage of graphene growth, S−Cu existed as a Cu phase containing dissolved S atoms (Figure S9). After graphene growth for 60 min, atomic S was almost exhausted (Figure S10). This result indicates that the S atoms dissolved in Cu were gradually eliminated by $H_2$ gas during graphene growth according to the following reaction[30]

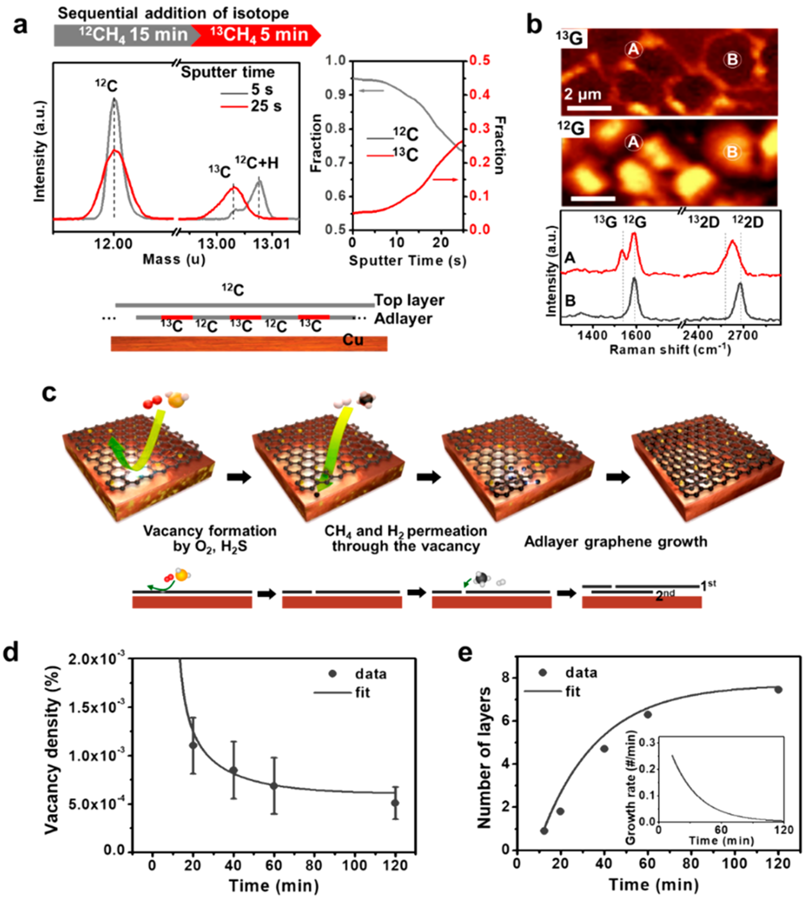

**Figure 2.** Growth and doping mechanism of S-graphene on S−Cu. (a) (Left) TOF-SIMS mass spectra of $^{12}$C and $^{13}$C after Cs$^+$ sputtering for 5 (gray) or 25 s (red). (Right) depth profiles for $^{12}$C (gray) and $^{13}$C (red). (b) Raman intensity map of $^{13}$G (top) and $^{12}$G (middle), and corresponding Raman spectra at the marked points (bottom). (c) Schematic diagram of the proposed mechanism of multilayer graphene growth and S doping. (d) Experimental (points) and simulated (line) vacancy concentration in S-graphene. (e) Number of graphene layers as a function of growth time. (Inset) Growth rate of graphene vs growth time.

$$\mathrm{S(in\ Cu) + H_2(g) \rightarrow H_2S(g)} \quad (1)$$

We suggest a mechanism (Figure 2c) for the growth of MLG with an S concentration gradient along the *c* axis. The $H_2S$ gas produced by reaction 1 can facilitate formation of vacancies in graphene with the aid of leakage oxygen ($O_2$) in the CVD chamber through the following reaction[31]

$$\mathrm{C(s) + O_2(g) + H_2S(g) \rightarrow COS(g) + H_2O(g)} \quad (2)$$

Reaction 2 produces vacancies in the formed graphene layer, and then $CH_4$ and $H_2$ gases permeate through these vacancies to form MLG beneath the initially formed graphene layer. As the growth of graphene proceeds, the rate of vacancy formation in graphene gradually decreases because the S concentration in S−Cu decreases, resulting in a decrease in the rate at which additional graphene layers form. The gradient of doping in S-graphene can be explained similarly, i.e., in terms of the decrease in the S concentration in Cu during graphene growth. The physisorption of S on graphene occurs through the following process

$$\mathrm{S}_n\ \mathrm{(on\ Cu) + graphene \rightarrow graphene\text{-}S}_n\ (n = 1, 2, 3) \quad (3)$$

As the concentration of S on the Cu surface decreases over time, the rate of reaction 3 also decreases. Therefore, the extent of S doping is high in the graphene formed initially (the upper layer) and relatively low in the graphene-formed later (the lower layer), so a gradient forms in the S-doping level along the *c* axis in the MLG.

We developed a growth kinetics model that takes reactions 1 and 2 into account and compared its predictions with the experimental data (Figure S11−S13). The measured average vacancy concentrations, $N_V/N_C$ (Figure 2d), and the number of graphene layers with growth time (Figure 2e) were in good agreement with the simulated values. The average vacancy concentration in graphene decreased as the growth of graphene proceeded; this trend indicates that the rate of vacancy formation decreased in the graphene layers grown later. Therefore, the growth rate of MLG decreased over time in accord with the decline in the vacancy concentration, i.e., the concentration of permeation centers for carbon precursors; this trend is consistent with the proposed growth mechanism.

**Atomic and Electronic Structure of S-Graphene.** The C 1s XPS spectrum of S-graphene can be deconvoluted into three peaks (Figure 3a): graphitic carbons (∼284.6 eV), carbons in C−O or C−S bonds (∼286.1 eV), and carbons in C═O bonds (∼289.0 eV). The portion of nongraphitic carbons is negligibly small compared to that of graphitic carbons, which also indicates that the number of chemisorbed sulfur compounds on S-graphene is negligible. The S $2p_{3/2}$ (∼164 eV) and S $2p_{1/2}$ peaks (∼165 eV) in the S 2p XPS spectrum of S-graphene transferred onto the $SiO_2$ substrate are

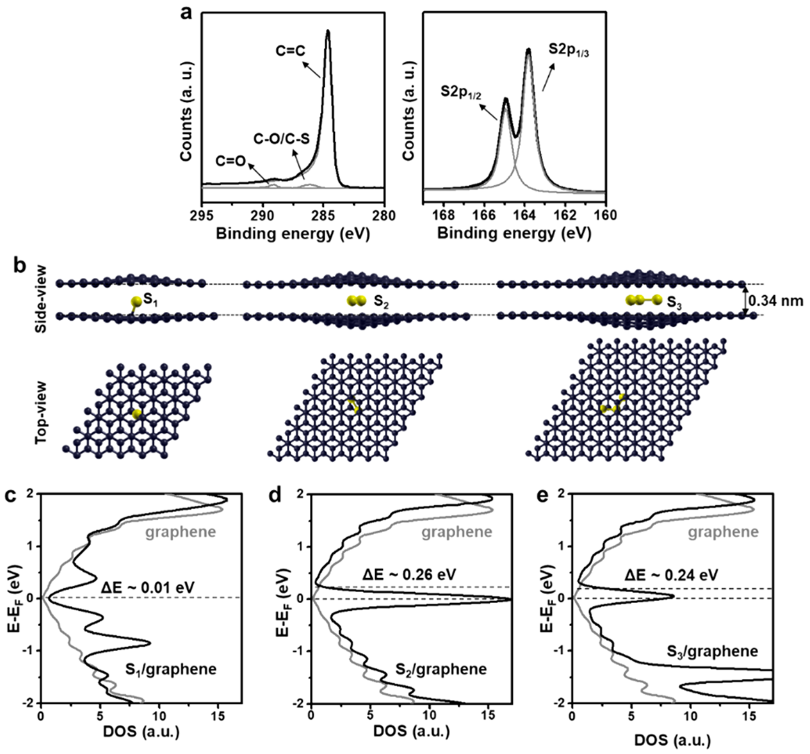

**Figure 3.** Atomic and electronic structures of S-graphene. (a) XPS C 1s (top) and S 2p (bottom) spectra for S-graphene. (b) Calculated structures of graphene/$S_1$/graphene (left), graphene/$S_2$/graphene (middle), and graphene/$S_3$/graphene (right). Calculated densities of states: (c) $S_1$-graphene, (d) $S_2$-graphene, and (e) $S_3$-graphene; density of states for pristine graphene (gray) is also shown.

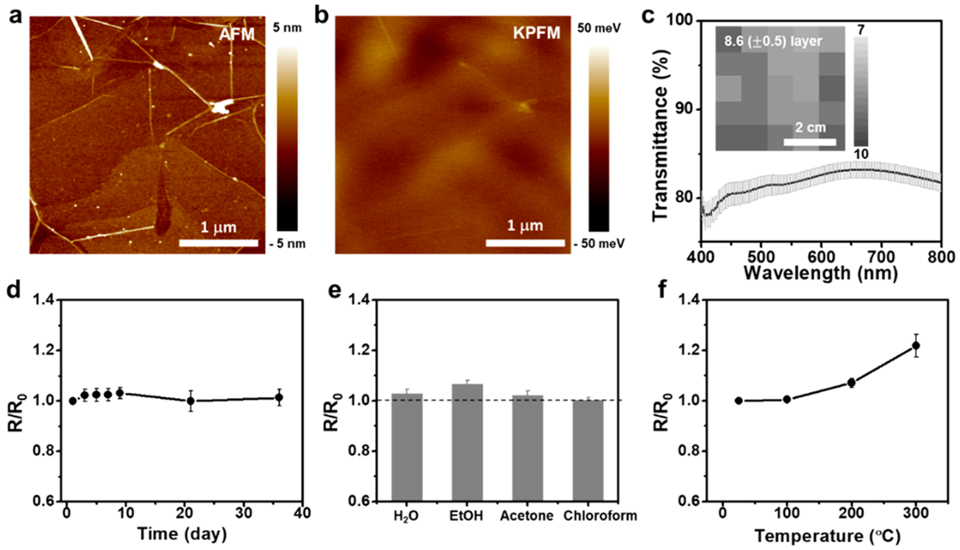

**Figure 4.** Uniformity and stability of S-graphene. (a) AFM and (b) KPFM images of S-graphene. (c) Average transmittance of the spectrum estimated from 25 S-graphene samples. (Inset) Thickness map of large-area S-graphene. Error bars indicate standard deviations. Variations in the electrical resistance of S-graphene: (d) during exposure to air, (e) after exposure to chemical solvents. (f) Variation with annealing temperature in the electrical resistance of S-graphene after thermal annealing under vacuum for 1 h.

sharply split, in contrast to the S 2p XPS spectra of bulk $\alpha$-$S_8$[32] or of substituted sulfur atoms in graphene, in which cases there are broad overlaps of the two peaks.[33] In addition, no oxidized sulfur peak (~168 eV) is evident.[33] The absence of the Cu 2p spectrum (Figure S14) indicates that the doping effect by residual sulfurized Cu compound is negligible. Therefore, the shape of the S 2p XPS spectrum indicates that small sulfur clusters ($S_1$, $S_2$, $S_3$) are intercalated between the graphene layers and that the $sp^2$ bonding of graphene is preserved.

To gain a deeper understanding of the structure of S-graphene, we performed density functional theory (DFT) calculations on bilayer graphene structures with intercalated $S_1$, $S_2$, and $S_3$ molecules (~1 atom % S in graphene) (Figure S15). The Bernal stacking of graphene is not affected by such intercalation in all cases; however, the interlayer distance is increased by the intercalation of an $S_n$ molecule (Figure 3b). This result is consistent with the slightly expanded *d* spacing of S-graphene evident in the HR-TEM images (Figure S16); the

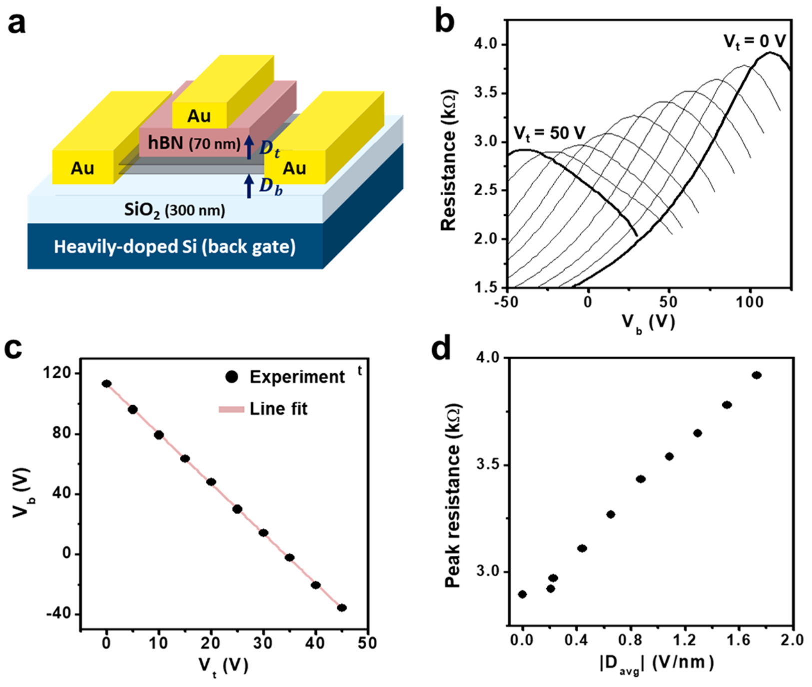

**Figure 5.** Dual-gate graphene field-effect transistor. (a) Schematic cross-section of the device. (b) FET resistance as a function of $V_b$ at $V_t$ in 5 V steps from 0 to 50 V. (c) $V_b$ and $V_t$ values that correspond to the peak resistance. (d) Peak resistances as a function of $D_{avg}$.

*d* spacing of the upper layer was found to be larger than that of graphite, whereas that of the lower layer is barely affected by intercalation. To elucidate how the physisorption of $S_n$ clusters induces the p-doping of graphene, we calculated the densities of states of graphene with $S_1$, $S_2$, and $S_3$ and compared them with that of pristine graphene (Figure 3c−e). The calculated Fermi levels are 0.01, 0.26, and 0.24 eV lower in S-graphene than in pristine graphene for $S_1$, $S_2$, and $S_3$, respectively. The negligible p-doping of graphene by $S_1$ arises because the electronegativity of the sulfur atom is similar to that of the carbon atom. The presence of localized, S-like states in the density of states of S-graphene in all cases implies that the orbitals of S are localized, which indicates that sulfur is physisorbed onto graphene.

**Uniformity and Stability of S-Graphene.** In addition, we evaluated the uniformity and stability of synthesized S-graphene (8.6 layers). First, the thickness uniformity of the sample on the microscale (3 $\mu$m × 3 $\mu$m) was evaluated using atomic force microscopy (Figure 4a). The root-mean-square roughness of the sample was found to be 0.5 nm, which corresponds to 1.4 layers. This high uniformity of the thick multilayer graphene grown with CVD was achieved because the growth in this method arises through surface-mediated reactions on the Cu surface, not through segregation or precipitation of C atoms. The doping uniformity of S-graphene was investigated using Kelvin probe force microscopy, which measures the potential offset between a probe tip and the S-graphene surface (Figure 4b). The standard deviation of the potential offset was found to be 5 meV, which indicates high doping uniformity. We also assessed the thickness uniformity of S-graphene over a large area. S-graphene/Cu foil (5 cm × 5 cm) was cut into 25 pieces (1 cm × 1 cm). We measured the transmittance of each sample after transfer to a glass substrate at $\lambda$ = 550 nm (Figure 4c). The average transmittance at $\lambda$ = 550 nm was found to be 80.2% (8.6 layers) with a standard deviation of 1.6% (0.5 layer).

To quantify the long-term doping stability of S-graphene, we measured the electrical resistance of a S-graphene sample exposed to air (Figure 4d). For 35 days, the electrical resistance of S-graphene remained constant. In addition, we assessed the chemical stability of S-graphene by dipping it into various chemical solvents: polar protic solvents (deionized water, ethanol), a polar aprotic solvent (acetone), and a nonpolar solvent (chloroform) (Figure 4e). All of the solvents were found to have negligible effects on the resistance of S-graphene. The thermal stability of S-graphene was also evaluated. We annealed S-graphene samples at 100, 200, and 300 °C for 1 h and then cooled the samples to room temperature before measuring their electrical resistances (Figure 4f). The resistance of S-graphene barely changes when the annealing temperature is lower than 300 °C and increases by 20% after thermal annealing at 300 °C, which demonstrates the high thermal stability of S-graphene. In S-graphene, the dopants are not simply physisorbed but intercalated, which results in a high stability that is hard to achieve with postgrowth chemical doping.

**Band Gap of Bilayer S-Graphene.** Bernal-stacked bilayer graphene is the most intensively studied multilayer graphene because it has a tunable band gap under an external electric field. To demonstrate the possibility using our method of preparing Bernal-stacked bilayer graphene with a band gap, we synthesized bilayer S-graphene, and its doping structure was investigated by fabricating dual-gate graphene FETs (Figure 5a). The top ($D_t$) and bottom ($D_b$) displacement fields determine the net carrier doping and band gap of graphene; a nonzero $\delta D = D_b - D_t$ leads to a net carrier doping, whereas a nonzero $D_{avg} = (D_b + D_t)/2$ generates asymmetry in the on-site energies between the graphene layers, which yields a band gap. In our samples, $D_b = \varepsilon_b(V_b - V_{b0})/d_b$ and $D_t = -\varepsilon_t(V_t - V_{t0})/d_t$, where $\varepsilon_b = 3.9$, $d_b$ = 300 nm for thermal $SiO_2$, $d_t$ = 70 nm for hexagonal boron nitride (hBN) dielectrics, and $V_0$ is the effective offset voltage. The dielectric constant $\varepsilon_t$ of hBN was

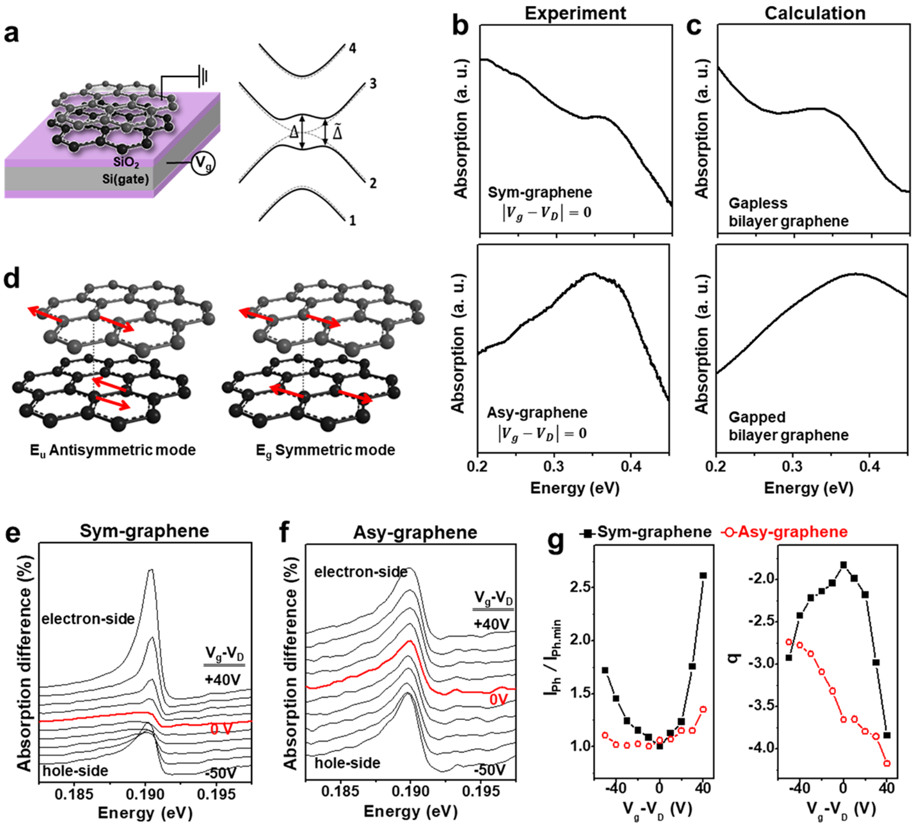

**Figure 6.** Infrared absorption of Sym-graphene and Asy-graphene. (a) Schematic diagrams of the infrared absorption experiment (left) and the band structure of Bernal-stacked bilayer graphene (right). Arrows: electronic transitions discussed in the text: ($\Delta$) energy asymmetry between graphene layers; ($\tilde{\Delta}$) optical band gap. IR absorption spectra in the range from 0.2 to 0.45 eV for Sym-graphene (upper) and Asy-graphene (lower) at their CNP: (b) experimental and (c) calculated. (d) $E_u$ antisymmetric-mode (left) and $E_g$ symmetric-mode (right) phonons. Gate-tunable IR absorption spectra at approximately 0.19 eV for (e) Sym-graphene and (f) Asy-graphene after subtraction of the background attributable to electronic transitions. (g) Fitted $I_{ph}$ normalized by its minimum value (left) and $q$ as a function of $V_g$ (right) for Sym-graphene (black filled squares) and Asy-graphene (red open circles).

measured to be 3.0. The offset voltages can be determined by identifying the lowest FET resistance, which is obtained at the charge neutrality point (CNP) for zero band gap graphene, i.e., $D_b = D_t = 0$. Therefore, the $V_b$ and $V_t$ values that correspond to the lowest resistance are the offset voltages. In our sample, these parameters were estimated to have values of $V_{b0} = -20.6$ V and $V_{t0} = 40$ V. The peak resistance increases as $D_{avg}$ increases (Figure 5d); this trend indicates the presence of a tunable band gap in our bilayer S-graphene, which in turn corroborates our claim that S-graphene has Bernal-like stacking.[34] The doping structure of the synthesized bilayer graphene sample can be determined from $V_{b0}$ and $V_{t0}$. The values $\delta D = -1.45$ V nm$^{-1}$ and $D_{avg} = 1.0$ V nm$^{-1}$ were estimated for ungated graphene ($V_b = V_t = 0$). Under our definition of $D_b$ and $D_t$, the negative value of $\delta D$ corresponds to the p-doping of graphene and the positive $D_{avg}$ value indicates that the top layer graphene is more p-doped than the bottom layer; this result clearly confirms the presence of a gradient in the doping that generates the vertical electric field in S-graphene.

The electronic structure of bilayer S-graphene was further investigated by performing infrared (IR) absorption experiments because optical measurements of electronic structures of graphene are less affected by charged impurities or defects than electrical measurements.[34]

The IR absorption method is a suitable method to investigate the electronic structure of polycrystalline CVD-grown graphene because it provides the average characteristic in large area while nano-angle-resolved photoemission spectroscopy provides a direct but local feature of graphene. We synthesized bilayer graphene on S−Cu under two extreme growth conditions (Figure S17), so that one graphene sample exhibited negligible asymmetry in the on-site energy difference, $\Delta$, between two graphene layers (Sym-graphene) and the other sample exhibited a significant $\Delta$ between the top and the bottom layers (Asy-graphene). We then compared the IR absorption behaviors of the two samples.[35,36]

The graphene samples were transferred onto a 300 nm thick $SiO_2$/Si/300 nm thick $SiO_2$ substrate, and then the electrical resistances and IR spectra of the graphene samples were obtained during gating (Figure 6a). The CNP $V_D$ was 20 V for Sym-graphene and 70 V for Asy-graphene (Figure S18). An illustration of electronic structure of bilayer graphene shows possible optical transitions. Bands 1 and 2 correspond to the second highest and the highest conduction band, respectively, and Band 3 and 4 correspond to the lowest and the second lowest valence band of graphene, respectively. The 2 → 3 electronic transitions are dominant in the IR absorption spectra (Figure 6b) of the graphene samples at the CNP for the range from 0.2 to 0.45 eV because of Pauli blocking of the 1 → 2 and 3 → 4 transitions. For Sym-graphene, the IR absorption intensity decreases monotonically as the photon energy increases, which is expected from 2 → 3 transition of gapless Bernal-stacked bilayer graphene.[37] Our calculated

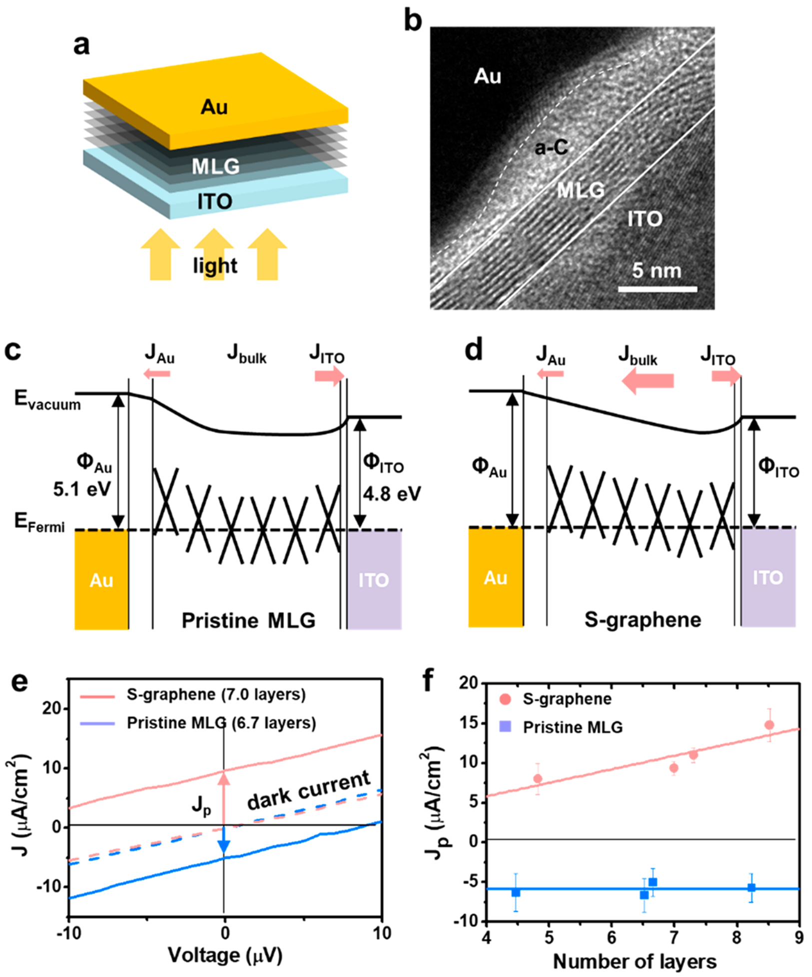

**Figure 7.** Vertical photovoltaic effect in S-graphene. (a) Structure and (b) cross-sectional HRTEM image of a Au/graphene/ITO photovoltaic device. Schematic band diagrams of the devices at equilibrium: (c) Au/pristine MLG/ITO and (d) Au/S-graphene/ITO. (e) Photoresponses of the photovoltaic devices under one-sun illumination. (f) Photocurrent levels in the Au/pristine MLG/ITO (blue) and Au/S-graphene/ITO devices (red) as a function of graphene thickness.

absorption spectrum (Figure 6c, top) for a nearly gapless bilayer graphene reproduces the observed absorption spectrum.

In contrast, the IR absorption spectrum of Asy-graphene at the CNP (Figure 6b, bottom) shows a broad absorption peak near 0.35 eV. This observation demonstrates that at the CNP Asy-graphene has a large Δ. The calculated absorption spectrum of bilayer graphene matches the observed absorption spectrum satisfactorily only for $\Delta > 0.4$ eV (Figure 6c, bottom; Figure S18). In addition to the differences in the IR absorptions between Sym-graphene and Asy-graphene in the range from 0.2 to 0.45 eV at the CNP, their gate voltage-dependent absorption behaviors also clearly differ (Figure S20).

We also analyzed the absorption of G-mode phonons (∼0.19 eV) by the Sym-graphene and Asy-graphene samples (Figure 6d) to further investigate their electronic structures. For undoped Bernal-stacked bilayer graphene, the antisymmetric-mode phonons (Figure 6d, left) are IR active whereas the symmetric-mode phonons (Figure 6d, right) are IR inactive because they carry zero dipole moment. In the presence of an on-site energy difference Δ, the inversion symmetry of bilayer graphene is broken, and the symmetric-mode phonons also become IR active. In this case, both the antisymmetric- and the symmetric-mode phonons are not normal modes, but the IR absorption can be treated as the sum of the IR absorptions by the antisymmetric- and symmetric-mode phonons. The relative contributions of the antisymmetric and symmetric phonons to the phonon peak and thus to the IR absorption behaviors near 0.19 eV are determined by the Fermi level and the size of the band gap of graphene.[38] In particular, when symmetric-mode phonons are coupled with the 2 → 3 electronic transition, Fano interference can be observed. Therefore, the IR absorption behavior near 0.19 eV can be engineered by tuning Δ and the Fermi level.

For Sym-graphene, when $|V_g - V_D|$ is close to 0 V, the absorption spectrum near 0.19 eV is featureless (Figure 6e). When a finite $|V_g - V_D|$ is applied to the graphene, a peak that is highly asymmetric with respect to a Lorentzian profile appears in the absorption spectrum; this feature indicates the occurrence of Fano interference between the continuum electronic states and the discrete phonon states.[39,40] The Fano line shape can be fitted with the following equation

$$\Delta A(\omega) = I_{\mathrm{ph}}\left[\frac{q^2 + 2qz - 1}{q^2(1 + z^2)}\right] \tag{4}$$

where $\Delta A(\omega)$ is the absorption difference at $E = \hbar\omega$, $I_{\mathrm{ph}}$ is a prefactor that represents the peak intensity, $q$ is a dimensionless Fano parameter that represents the asymmetry of the peak, and $z = 2(\omega - \omega_0)/\Gamma$, where $\omega_0$ is the phonon frequency and $\Gamma$ is the line broadening of the phonon. For Sym-graphene, the fitting parameter $I_{\mathrm{Ph}}$ gradually increases as $|V_g - V_D|$ increases (Figure 6g, left). This variation implies that the phonon strength of the antisymmetric mode relative to that of the symmetric mode increases as $|V_g - V_D|$ increases; the phonon strength of the antisymmetric mode is determined by the coupling with the 1 → 2 or 3 → 4 transitions, which is proportional to the Fermi level of graphene, whereas the phonon strength of the symmetric mode is mainly determined by $\Delta$ and is at its maximum when $\Delta \approx \hbar\omega_0$.[41] The Fano parameter $|q|$ also increases as the Fermi level departs from the CNP (Figure 6g, right), which is attributed to the increase in the relative phonon strength of the antisymmetric mode with $|V_g - V_D|$; in contrast to the symmetric-mode phonon, which can couple with 2 → 3 electronic transitions and thus give rise to a finite $|q|$, the antisymmetric phonon cannot couple with 2 → 3 electronic transitions, so the Fano asymmetry is negligible ($|q| \to \infty$). The observed $V_g$ dependence of the relative phonon strength reflects the $V_g$-dependent electronic structure of bilayer graphene with a small $\Delta$, as expected for Sym-graphene.

The $V_g$ dependence of the Asy-graphene absorption spectra (Figure 6f) is different from that of the Sym-graphene absorption spectra. Fano interference is evident over a wide range of $|V_g - V_D|$, and the peak intensity has a weak $V_g$ dependence (Figure 6g, left). These results indicate that $\Delta$ is significant in Asy-graphene for the measured range of $|V_g - V_D|$ and that in contrast to Sym-graphene, the IR absorption of the symmetric-mode phonons predominates over that of antisymmetric-mode phonons for Asy-graphene.[41] $|q|$ is lowest for $V_g - V_D = -50$ V and increases as $V_g$ increases. The increase in $|q|$ arising from symmetric-mode phonons can occur when the 2 → 3 electronic transitions at $\hbar\omega_0$ decrease or when $\Delta$ between the graphene layers becomes larger than $\hbar\omega_0$; this trend implies that $\Delta$ becomes larger than $\hbar\omega_0$ as $V_g$ increases (Figure 6g, right). The absence of negative phonon absorption in the spectra and the weak $V_g$ dependence of the peak intensity suggest that the band gap of Asy-graphene is >0.2 eV for the whole measured range of $|V_g - V_D|$.[41] These behaviors of Asy-graphene are consistent with the doping state of Asy-graphene, i.e., the upper layer is significantly more p-doped than the lower layer in the ungated state; more negative charges accumulate in the lower layer as $V_g$ increases, which results in an increase in $\Delta$ with $V_g$.

**Vertical Photovoltaic Effect in Multilayer S-Graphene.** In addition to the tunablility of electronic structure at the synthesis stage, our synthesis method of S-graphene enabled us to prepare thick multilayer graphene exhibiting a vertical photovoltaic effect, which is hard to achieve with conventional multilayer graphene due to a strong interlayer screening effect.[26] We compared the photovoltaic characteristic of MLG depending on the existence of an internal E-field by measuring the photocurrent of a Au/MLG/ITO vertically structured device under one-sun illumination (Figure 7a and 7b). S-graphene has an internal E-field, while the pristine MLG which was prepared by CVD on Cu foil with thin Ni on back of it has not.[42]

Both pristine MLG and S-graphene have Bernal-like stacking so that photogenerated carriers flow through graphene both by band conduction and by band hopping conduction.[43] In contrast to lateral metal/graphene/metal devices in which photocurrent is generated by combination of the thermoelectric Seebeck effect,[44,45] the bolometric effect,[46,47] and the photovoltaic effect,[48] the photocurrent of vertical Au/graphene/ITO devices at zero bias is due solely to the photovoltaic effect because there is no temperature gradient in the vertical direction in the device under illumination.

Figure 7c and 7d shows the band diagrams of the Au/graphene/ITO structures at equilibrium. The work functions of Au and ITO are larger than that of graphene, so band bending occurs near the graphene/electrode junctions. Thus, negative photocurrent arises near the graphene/ITO junction ($-J_{\mathrm{ITO}}$), and positive photocurrent arises near the graphene/Au junction ($J_{\mathrm{Au}}$) at zero bias under illumination for both the pristine MLG and the S-graphene devices. In addition, positive photocurrent can be generated in the bulk region of MLG (the region between layers 2 and ($N - 1$) for $N$-layer MLG) ($J_{\mathrm{bulk}}$) if a sufficiently strong built-in E-field is present that separates photogenerated electrons and holes. In our devices, the contact of graphene with Au is relatively poor because of polymer residues on top of graphene (Figure 7b), which is caused during graphene transfer; thus, the total photocurrent of the device ($J_p$) at zero bias is determined by $J_{\mathrm{ITO}}$ and $J_{\mathrm{bulk}}$; $J_p \approx J_{\mathrm{bulk}} - J_{\mathrm{ITO}}$.

As shown in Figure 7e, the Au/pristine MLG/ITO device exhibits negative photocurrent under one-sun illumination, which indicates that $J_{\mathrm{ITO}}$ dominates $J_{\mathrm{bulk}}$. It means the E-field inside pristine MLG is not sufficiently strong to generate $J_{\mathrm{bulk}}$ despite the work function difference between Au and ITO. In addition, $J_p$ is independent of the thickness of pristine MLG (Figure 7f) even though thicker MLG absorbs more light, which means that the contribution of $J_{\mathrm{bulk}}$ to $J_p$ is very small.

In contrast to the pristine MLG device, the Au/S-graphene/ITO device exhibits positive $J_p$ under the same conditions (Figure 7e). $J_{\mathrm{ITO}}$ is essentially the same for pristine MLG and S-graphene, so the positive $J_p$ of the Au/S-graphene/ITO device is the result of $J_{\mathrm{bulk}}$ generated inside S-graphene. In contrast to the pristine MLG case, $J_p$ of the device increases as the thickness of S-graphene increases. This result shows that the photogenerated carriers inside S-graphene contribute to $J_p$, that is, the built-in E-field inside thick S-graphene is sufficiently strong to separate photogenerated electrons and holes. To the best of our knowledge, these results provide the first demonstration of vertical photovoltaic current in the bulk region of multilayer graphene under continuous-wave illumination; this current could be further enhanced by carrier multiplication in graphene with an ultrashort laser pulse.[49]

## ■ CONCLUSION

In summary, we proposed a method for the synthesis of MLG with a built-in E-field along the $c$ axis. By controlling the growth conditions, the thickness and E-field can be readily tuned over a wide range. Our dual-gate FET and IR absorption measurements have demonstrated the tunability of the electronic structure and enabled the determination of the optoelectronic properties of the synthesized bilayer graphene. Owing to its strong built-in E-field and Bernal-like stacking, multilayer S-graphene exhibits a vertical photovoltaic effect under continuous-wave illumination with visible light.

## ■ METHODS

**S-Graphene Growth.** Cu foil (25 μm thick, Alfa Aesar 99.999% purity) was annealed in a vacuum chamber with 10 sccm $H_2$ at 700 °C for 3 h to remove the surface Cu oxide layer. The Cu foil and a sulfur slice were put in another vacuum chamber. The Cu foil was positioned at the center of the heater, and the sulfur slice was positioned on the upper stream of the heater edge. The temperature was raised from RT to 120 °C and then held at 120 °C for 15 min to anneal the Cu foil. After a CuS layer had formed on the foil, the chamber was rapidly cooled to RT. The Cu foil covered with the CuS layer was moved to a CVD chamber, in which graphene was grown using a conventional graphene-growth recipe.

**Raman.** Raman measurements were conducted using a Witec alpha 300R Confocal Raman Spectrometer. The excitation laser had wavelength $\lambda$ = 488 nm for measurement of as-grown S-graphene and $\lambda$ = 532 nm for S-graphene after it had been transferred to the target substrate. Before the spectrum of S-graphene was measured, the Raman spectrum was calibrated with the Raman signature of Si at 520 $cm^{-1}$. The numerical aperture (NA) of the lens was 0.4 except the Raman G-peak intensity map for isotope labeling (NA = 0.9).

**TOF-SIMS.** The TOF-SIMS spectrum was obtained using TOF-SIMS 5-100 (Ion-tof). Cs-ion sputtering was conducted with an energy of 2 keV and current of 108 nA in an area of 300 × 300 $\mu m^2$. For the analysis, an energy of 30 keV and a current of 0.92 pA 100 × 100 $\mu m^2$ were set as analysis parameters.

**TEM.** The cross-sectional and in-plane TEM image and EELS S map of S-graphene were obtained using a JEOL JEM-2200FS (with Image Cs-corrector). The EDX spectrum was obtained using a JEOL JEM-2100F with Cs-corrected STEM. Copper was removed for all samples to exclude the existing S atoms in S−Cu.

**DFT Calculations.** DFT calculations for the optimized structure and corresponding DOS of $S_n$-graphene were performed using Quantum Espresso 6.3.0 versions 3 and 4 and Plain Augmented Waves (PAW) Ultrasoft pseudopotential from the PAL library. Calculation conditions are given in Figure S15. An independent particle approximation as implemented in YAMBO was applied for calculation of the absorption of bilayer graphene (Figure S19).

**Photovoltaics.** Synthesized thick S-graphene was transferred onto ITO-coated glass substrate using the conventional wet transfer method. The supporting PMMA layer was removed by dipping the assemblage in chloroform for 2 h. Then an Au electrode was deposited by thermal evaporation. S-graphene with different thicknesses was synthesized by adjusting the growth time. Dark current and photocurrent were measured using a semiconductor analyzer (Agilent B1500A) by averaging the current over time for each voltage step. The devices were mounted on an optical table in a Faraday cage with a small aperture for the laser beam and then illuminated at one sun using a solar simulator.

## ■ ASSOCIATED CONTENT

### Supporting Information

Details of synthesis of multilayer S-graphene on S−Cu and resulting transmittance, Atomic dis-tribution of S-graphene, SAED pattern, Raman and carrier transport property analysis, TOF-SIMS depth profile of IS/IC of inversely transferred S-graphene, UPS spectrum of S-graphene and pristine graphene, Reduction of sulfurized Cu and cross-sectional atomic distribution of S−Cu, Schematic diagram of graphene growth mechanism and doping mechanism on S−Cu, Thickness of S-graphene determined by initial CuS thickness, The Cu 2p XPS spectrum of transferred S-graphene on Si-wafer, DFT calculation for graphene structure with Sn (n∈{1,2,3}) molecule adsorbed or intercalated, and correspond-ing density of states, The *d*-spacing expansion of S-graphene, Work function depth profile of Sym-graphene and Asy-graphene, Vg-dependent current of Asy-graphene and Sym-graphene FET, DFT calculation for energy gap of bilayer gra-phene and associated absorption spectrum, Gate-tunable IR absorption peak near 0.35 eV, Conditions to synthesize S-graphene having various thickness and built-in electric field. The Supporting Information is available free of charge at https://pubs.acs.org/doi/10.1021/acs.chemmater.0c01145.

(PDF)

## ■ AUTHOR INFORMATION

### Corresponding Author

**Kilwon Cho** − *Department of Chemical Engineering, Pohang University of Science and Technology, Pohang 37673, Republic of Korea;* orcid.org/0000-0003-3321-3629;
Email: kwcho@postech.ac.kr

### Authors

**Min Seok Yoo** − *Department of Chemical Engineering, Pohang University of Science and Technology, Pohang 37673, Republic of Korea*
**Hyo Chan Lee** − *Department of Chemical Engineering, Pohang University of Science and Technology, Pohang 37673, Republic of Korea*
**Christoph Wolf** − *Center for Quantum Nanoscience, Institute for Basic Sciences (IBS), Seoul 03760, Republic of Korea*
**Nguyen Ngan Nguyen** − *Department of Chemical Engineering, Pohang University of Science and Technology, Pohang 37673, Republic of Korea*
**Do-Hyun Park** − *Department of Physics, Konkuk University, Seoul 05029, Republic of Korea*
**Jinsung Kim** − *Department of Chemical Engineering, Pohang University of Science and Technology, Pohang 37673, Republic of Korea*
**Eunho Lee** − *Department of Chemical Engineering, Pohang University of Science and Technology, Pohang 37673, Republic of Korea*
**Hyun-Jong Chung** − *Department of Physics, Konkuk University, Seoul 05029, Republic of Korea*

Complete contact information is available at:
https://pubs.acs.org/10.1021/acs.chemmater.0c01145

### Author Contributions

‡M.S.Y. and H.C.L.: These authors contributed equally to this work.

### Author Contributions

Experiments and data analysis were carried out mainly by M.S.Y. and H.C.L. under the supervision of K.C. C.W. conducted DFT calculations. AFM and KPFM were conducted and analyzed by N.N.N. Infrared spectroscopy experiments were carried out by J.K. and E.L. Fabrication and characterization of dual-gate FETs were carried out by D.-H.P. and H.-J.C.. M.S.Y. and H.C.L. wrote the manuscript under the supervision of K.C.

### Notes

The authors declare no competing financial interest.

## ■ ACKNOWLEDGMENTS

This work was supported by a grant from the Center for Advanced Soft Electronics under the Global Frontier Research Program of the Ministry of Science and ICT, Korea (Code No. 2011-0031628).

## ■ ABBREVIATIONS USED

CVD, chemical vapor deposition; MLG, multilayer graphene; E-field, electric-field; FETs, field-effect transistor; S-Cu, sulfurized and sulfur-dissolving Cu; S-graphene, S-doped multilayer graphene; TEM, transmission electron microscopy;

EELS, electron energy loss spectroscopy; TOF-SIMS, time-of-flight secondary ion mass spectrometry; UPS, ultraviolet photoelectron spectroscopy; XPS, X-ray photoemission spectroscopy; hBN, hexagonal boron nitride; CNP, charge neutrality point

## ■ REFERENCES

(1) Novoselov, K. S.; Fal'ko, V. I.; Colombo, L.; Gellert, P. R.; Schwab, M. G.; Kim, K. A roadmap for graphene. *Nature* **2012**, *490*, 192−200.

(2) Lundeberg, M. B.; Gao, Y. D.; Asgari, R.; Tan, C.; Van Duppen, B.; Autore, M.; Alonso-Gonzalez, P.; Woessner, A.; Watanabe, K.; Taniguchi, T.; Hillenbrand, R.; Hone, J.; Polini, M.; Koppens, F. H. L. Tuning quantum nonlocal effects in graphene plasmonics. *Science* **2017**, *357*, 187−190.

(3) Yang, Q.; Su, Y.; Chi, C.; Cherian, C. T.; Huang, K.; Kravets, V. G.; Wang, F. C.; Zhang, J. C.; Pratt, A.; Grigorenko, A. N.; Guinea, F.; Geim, A. K.; Nair, R. R. Ultrathin graphene-based membrane with precise molecular sieving and ultrafast solvent permeation. *Nat. Mater.* **2017**, *16*, 1198−1202.

(4) Mak, K. F.; Shan, J.; Heinz, T. F. Electronic Structure of Few-Layer Graphene: Experimental Demonstration of Strong Dependence on Stacking Sequence. *Phys. Rev. Lett.* **2010**, *104*, 176404.

(5) Freitag, M. GRAPHENE Trilayers unravelled. *Nat. Phys.* **2011**, *7*, 596−597.

(6) Nguyen, T. A.; Lee, J. U.; Yoon, D.; Cheong, H. Excitation Energy Dependent Raman Signatures of ABA- and ABC-stacked Few-layer Graphene. *Sci. Rep.* **2015**, *4*, 4630.

(7) Park, C.; Ryou, J.; Hong, S.; Sumpter, B. G.; Kim, G.; Yoon, M. Electronic Properties of Bilayer Graphene Strongly Coupled to Interlayer Stacking and an External Electric Field. *Phys. Rev. Lett.* **2015**, *115*, 015502.

(8) Li, J. I. A.; Tan, C.; Chen, S.; Zeng, Y.; Taniguchi, T.; Watanabe, K.; Hone, J.; Dean, C. R. Even-denominator fractional quantum Hall states in bilayer graphene. *Science* **2017**, *358*, 648−651.

(9) Cao, Y.; Fatemi, V.; Fang, S.; Watanabe, K.; Taniguchi, T.; Kaxiras, E.; Jarillo-Herrero, P. Unconventional superconductivity in magic-angle graphene superlattices. *Nature* **2018**, *556*, 43−50.

(10) McCann, E. Asymmetry gap in the electronic band structure of bilayer graphene. *Phys. Rev. B: Condens. Matter Mater. Phys.* **2006**, *74*, 161403.

(11) Zhang, Y. B.; Tang, T. T.; Girit, C.; Hao, Z.; Martin, M. C.; Zettl, A.; Crommie, M. F.; Shen, Y. R.; Wang, F. Direct observation of a widely tunable bandgap in bilayer graphene. *Nature* **2009**, *459*, 820−823.

(12) Kim, K. S.; Walter, A. L.; Moreschini, L.; Seyller, T.; Horn, K.; Rotenberg, E.; Bostwick, A. Coexisting massive and massless Dirac fermions in symmetry-broken bilayer graphene. *Nat. Mater.* **2013**, *12*, 887−892.

(13) Li, J.; Wang, K.; McFaul, K. J.; Zern, Z.; Ren, Y. F.; Watanabe, K.; Taniguchi, T.; Qiao, Z. H.; Zhu, J. Gate-controlled topological conducting channels in bilayer graphene. *Nat. Nanotechnol.* **2016**, *11*, 1060−1065.

(14) Pospischil, A.; Humer, M.; Furchi, M. M.; Bachmann, D.; Guider, R.; Fromherz, T.; Mueller, T. CMOS-compatible graphene photodetector covering all optical communication bands. *Nat. Photonics* **2013**, *7*, 892−896.

(15) Balandin, A. A. Low-frequency 1/f noise in graphene devices. *Nat. Nanotechnol.* **2013**, *8*, 549−555.

(16) Kim, C. J.; Sanchez-Castillo, A.; Ziegler, Z.; Ogawa, Y.; Noguez, C.; Park, J. Chiral atomically thin films. *Nat. Nanotechnol.* **2016**, *11*, 520−524.

(17) Ju, L.; Shi, Z. W.; Nair, N.; Lv, Y. C.; Jin, C. H.; Velasco, J.; Ojeda-Aristizabal, C.; Bechtel, H. A.; Martin, M. C.; Zettl, A.; Analytis, J.; Wang, F. Topological valley transport at bilayer graphene domain walls. *Nature* **2015**, *520*, 650−655.

(18) Kim, K. S.; Zhao, Y.; Jang, H.; Lee, S. Y.; Kim, J. M.; Kim, K. S.; Ahn, J. H.; Kim, P.; Choi, J. Y.; Hong, B. H. Large-scale pattern growth of graphene films for stretchable transparent electrodes. *Nature* **2009**, *457*, 706−710.

(19) Sun, Z. Z.; Yan, Z.; Yao, J.; Beitler, E.; Zhu, Y.; Tour, J. M. Growth of graphene from solid carbon sources. *Nature* **2010**, *468*, 549−552.

(20) Hao, Y. F.; Wang, L.; Liu, Y. Y.; Chen, H.; Wang, X. H.; Tan, C.; Nie, S.; Suk, J. W.; Jiang, T. F.; Liang, T. F.; Xiao, J. F.; Ye, W. J.; Dean, C. R.; Yakobson, B. I.; McCarty, K. F.; Kim, P.; Hone, J.; Colombo, L.; Ruoff, R. S. Oxygen-activated growth and bandgap tunability of large single-crystal bilayer graphene. *Nat. Nanotechnol.* **2016**, *11*, 426−431.

(21) Lee, H. C.; Jo, S. B.; Lee, E.; Yoo, M. S.; Kim, H. H.; Lee, S. K.; Lee, W. H.; Cho, K. Facet-Mediated Growth of High-Quality Monolayer Graphene on Arbitrarily Rough Copper Surfaces. *Adv. Mater.* **2016**, *28*, 2010−2017.

(22) Ta, H. Q.; Perello, D. J.; Duong, D. L.; Han, G. H.; Gorantla, S.; Nguyen, V. L.; Bachmatiuk, A.; Rotkin, S. V.; Lee, Y. H.; Rummeli, M. H. Stranski-Krastanov and Volmer-Weber CVD Growth Regimes To Control the Stacking Order in Bilayer Graphene. *Nano Lett.* **2016**, *16*, 6403−6410.

(23) Ohta, T.; Bostwick, A.; Seyller, T.; Horn, K.; Rotenberg, E. Controlling the electronic structure of bilayer graphene. *Science* **2006**, *313*, 951−954.

(24) Zhan, D.; Sun, L.; Ni, Z. H.; Liu, L.; Fan, X. F.; Wang, Y. Y.; Yu, T.; Lam, Y. M.; Huang, W.; Shen, Z. X. $FeCl_3$-Based Few-Layer Graphene Intercalation Compounds: Single Linear Dispersion Electronic Band Structure and Strong Charge Transfer Doping. *Adv. Funct. Mater.* **2010**, *20*, 3504−3509.

(25) Park, J.; Jo, S. B.; Yu, Y. J.; Kim, Y.; Yang, W.; Lee, W. H.; Kim, H. H.; Hong, B. H.; Kim, P.; Cho, K.; Kim, K. S. Single-Gate Bandgap Opening of Bilayer Graphene by Dual Molecular Doping. *Adv. Mater.* **2012**, *24*, 407−411.

(26) Kuroda, M. A.; Tersoff, J.; Martyna, G. J. Nonlinear Screening in Multilayer Graphene Systems. *Phys. Rev. Lett.* **2011**, *106*, 116804.

(27) Meyer, J. C.; Geim, A. K.; Katsnelson, M. I.; Novoselov, K. S.; Booth, T. J.; Roth, S. The structure of suspended graphene sheets. *Nature* **2007**, *446*, 60−63.

(28) Cancado, L. G.; Jorio, A.; Ferreira, E. H. M.; Stavale, F.; Achete, C. A.; Capaz, R. B.; Moutinho, M. V. O.; Lombardo, A.; Kulmala, T. S.; Ferrari, A. C. Quantifying Defects in Graphene via Raman Spectroscopy at Different Excitation Energies. *Nano Lett.* **2011**, *11*, 3190−3196.

(29) Eckmann, A.; Felten, A.; Mishchenko, A.; Britnell, L.; Krupke, R.; Novoselov, K. S.; Casiraghi, C. Probing the Nature of Defects in Graphene by Raman Spectroscopy. *Nano Lett.* **2012**, *12*, 3925−3930.

(30) Rao, Y. K.; Bagheri, H. Reduction of copper(I) sulfide with hydrogen and the morphology of Cu(s) product. *React. Solids* **1988**, *5*, 29−51.

(31) Jeong, T.; Kim, W. Y.; Hahn, Y. B. A new purification method of single-wall carbon nanotubes using $H_2S$ and $O_2$ mixture gas. *Chem. Phys. Lett.* **2001**, *344*, 18−22.

(32) Fujimori, T.; Morelos-Gomez, A.; Zhu, Z.; Muramatsu, H.; Futamura, R.; Urita, K.; Terrones, M.; Hayashi, T.; Endo, M.; Young Hong, S.; Chul Choi, Y.; Tomanek, D.; Kaneko, K. Conducting linear chains of sulphur inside carbon nanotubes. *Nat. Commun.* **2013**, *4*, 2162.

(33) Quan, B.; Yu, S. H.; Chung, D. Y.; Jin, A.; Park, J. H.; Sung, Y. E.; Piao, Y. Single source precursor-based solvothermal synthesis of heteroatom-doped graphene and its energy storage and conversion applications. *Sci. Rep.* **2015**, *4*, 5639.

(34) Min, H.; Abergel, D. S. L.; Hwang, E. H.; Das Sarma, S. Optical and transport gaps in gated bilayer graphene. *Phys. Rev. B: Condens. Matter Mater. Phys.* **2011**, *84*, 041406.

(35) Kuzmenko, A. B.; Benfatto, L.; Cappelluti, E.; Crassee, I.; van der Marel, D.; Blake, P.; Novoselov, K. S.; Geim, A. K. Gate Tunable Infrared Phonon Anomalies in Bilayer Graphene. *Phys. Rev. Lett.* **2009**, *103*, 116804.

(36) Li, Z. Q.; Henriksen, E. A.; Jiang, Z.; Hao, Z.; Martin, M. C.; Kim, P.; Stormer, H. L.; Basov, D. N. Band Structure Asymmetry of

Bilayer Graphene Revealed by Infrared Spectroscopy. *Phys. Rev. Lett.* **2009**, *102*, 037403.

(37) Kadi, F.; Malic, E. Optical properties of Bernal-stacked bilayer graphene: A theoretical study. *Phys. Rev. B: Condens. Matter Mater. Phys.* **2014**, *89*, 045419.

(38) Cappelluti, E.; Benfatto, L.; Kuzmenko, A. B. Phonon switching and combined Fano-Rice effect in optical spectra of bilayer graphene. *Phys. Rev. B: Condens. Matter Mater. Phys.* **2010**, *82*, 041402R.

(39) Tang, T. T.; Zhang, Y. B.; Park, C. H.; Geng, B. S.; Girit, C.; Hao, Z.; Martin, M. C.; Zettl, A.; Crommie, M. F.; Louie, S. G.; Shen, Y. R.; Wang, F. A tunable phonon-exciton Fano system in bilayer graphene. *Nat. Nanotechnol.* **2010**, *5*, 32−36.

(40) Low, T.; Guinea, F.; Yan, H.; Xia, F.; Avouris, P. Novel Midinfrared Plasmonic Properties of Bilayer Graphene. *Phys. Rev. Lett.* **2014**, *112*, 116801.

(41) Cappelluti, E.; Benfatto, L.; Manzardo, M.; Kuzmenko, A. B. Charged-phonon theory and Fano effect in the optical spectroscopy of bilayer graphene. *Phys. Rev. B: Condens. Matter Mater. Phys.* **2012**, *86*, 115439.

(42) Yoo, M. S.; Lee, H. C.; Lee, S.; Lee, S. B.; Lee, N. S.; Cho, K. Chemical Vapor Deposition of Bernal-Stacked Graphene on a Cu Surface by Breaking the Carbon Solubility Symmetry in Cu Foils. *Adv. Mater.* **2017**, *29*, 1700753.

(43) Sugihara, K. c-axis conduction in graphite intercalation compounds. *Phys. Rev. B: Condens. Matter Mater. Phys.* **1988**, *37*, 4752.

(44) Gabor, N. M.; Song, J. C.; Ma, Q.; Nair, N. L.; Taychatanapat, T.; Watanabe, K.; Taniguchi, T.; Levitov, L. S.; Jarillo-Herrero, P. Hot carrier-assisted intrinsic photoresponse in graphene. *Science* **2011**, *334*, 648−652.

(45) Xu, X.; Gabor, N. M.; Alden, J. S.; van der Zande, A. M.; McEuen, P. L. Photo-thermoelectric effect at a graphene interface junction. *Nano Lett.* **2010**, *10*, 562−566.

(46) Yan, J.; Kim, M. H.; Elle, J. A.; Sushkov, A. B.; Jenkins, G. S.; Milchberg, H. M.; Fuhrer, M. S.; Drew, H. D. Dual-gated bilayer graphene hot-electron bolometer. *Nat. Nanotechnol.* **2012**, *7*, 472−478.

(47) Freitag, M.; Low, T.; Xia, F.; Avouris, P. Photoconductivity of biased graphene. *Nat. Photonics* **2013**, *7*, 53−59.

(48) Lee, E. J. H.; Balasubramanian, K.; Weitz, R. T.; Burghard, M.; Kern, K. Contact and edge effects in graphene devices. *Nat. Nanotechnol.* **2008**, *3*, 486−490.

(49) Chen, J.-J.; Wang, Q.; Meng, J.; Ke, X.; Tendeloo, G. V.; Bie, Y.-Q.; Liu, J.; Liu, K.; Liao, Z.-M.; Sun, D.; Yu, D. Photovoltaic Effect and Evidence of Carrier Multiplication in Graphene Vertical Homojunctions with Asymmetrical Metal Contacts. *ACS Nano* **2015**, *9*, 8851−8858.

https://dx.doi.org/10.1021/acs.chemmater.0c01145